**PAPER**

# Below- and near-threshold harmonic generation from multiple orbitals

View the article online for updates and enhancements.

# Below- and near-threshold harmonic generation from multiple orbitals

**Jie Long**[1] , **Yuhang Chen**[1], **Xiaosong Zhu**[1,*] , **Lixin He**[1], **Pengfei Lan**[1,*] **and Peixiang Lu**[1,2]

[1] Wuhan National Laboratory for Optoelectronics and School of Physics, Huazhong University of Science and Technology, Wuhan 430074, People's Republic of China
[2] Optical Valley Laboratory, Hubei 430074, People's Republic of China

E-mail: zhuxiaosong@hust.edu.cn and pengfeilan@hust.edu.cn

## Abstract

We report an unexplored observation of multi-orbital contribution in the below- and near-threshold harmonic generation of aligned molecules. A typical pump–probe configuration is used in our experiments. By scanning the time delay and crossing angle of polarization directions between the pump and probe pulses, we find that the harmonic yield in this region exhibits abnormal intensity-dependent modulation patterns. Further comparison and analysis show that this observation can be interpreted as due to the contribution of deeper-lying molecular orbitals, which are much more prominent than in the above-threshold region and can overall surpass the contribution of the highest occupied molecular orbital, leading to reversed modulation patterns. The particular importance of the deeper-lying orbitals in this regime is closely related to the multi-photon excitation pathways involved in the generation process. Our work will advance further investigations on the mechanism of below- and near-threshold harmonic generation.

Keywords: multi-orbital contribution, multi-photon excitation pathways, below- and near-threshold harmonic generation

(Some figures may appear in colour only in the online journal)

## 1. Introduction

High-order harmonic generation (HHG) is one of the most fundamental phenomena in the interaction of strong laser field and matter, and has greatly promoted the advance of novel ultrafast light sources [1–4] and ultrafast detection [5, 6]. For harmonics above the ionization threshold, the HHG process can be explained by a semiclassical three-step model: ionization, propagation and photorecombination of an active electron in the strong driving field [7, 8]. In the case of aligned molecules, the tunnel ionization [9, 10] and recombination [11, 12] steps are anisotropic, and are determined by the structure of the contributing molecular orbitals. Since these anisotropic features will be displayed in the harmonic spectrum, one can reveal encoded information about the molecular orbitals from the harmonic spectrum. Recently, spectroscopy techniques based on the harmonic spectrum have been widely applied in the realm of ultrafast science [13–18].

Most spectroscopy techniques take only the highest occupied molecular orbital (HOMO) into account because it is generally considered that the contribution of HOMO dominates in HHG. However, more and more investigations have proposed that multi-electron effects, including multichannel dynamics [19–22] and electron correlation [23–25], are inevitably involved in HHG. These complex dynamics are responsible for the emission of elliptically polarized harmonics from aligned molecules in a linearly polarized driving field [26], and are indispensable for the cross-section reconstruction [27] and the tomographic reconstruction of deeper-lying molecular orbitals [24, 28]. Early observations of HHG from the deeper-lying orbitals are generally in the cutoff region [29], where

the relative contribution of deeper-lying molecular orbitals is greater because of its wider harmonic spectrum. The contribution of deeper-lying orbitals is manifested in the plateau region too, where the identification of contributing orbitals is generally realized by the intensity-dependent interference minima in the harmonic spectrum. From the position of these interference minima and their variation with the driving intensity, one can reveal the attosecond multi-electron dynamics, including electron rearrangement upon ionization [30] and multichannel coupling [31].

Turning to the generation of below- and near-threshold harmonics, the underlying physics could be much more complicated [32, 33]. It has been shown that the parent ion potential [34–36] and excited states [37, 38] can have an unneglectable impact on the harmonic generation in this region. Two main contributions to the below- and near-harmonic generation, known as the long and short trajectory, can also be identified [35, 39]. While the long trajectories can be understood similarly to the standard three-step picture of HHG, the short trajectory is quite different; it is dominated by electrons initially excited through multi-photon excitation pathways and evolves closely around the core [39]. Some novel phenomena, such as the anomalous ellipticity dependence of certain below-threshold harmonics [39–43] and the negative dispersion observed in the below-threshold harmonics [44], have been reported in the past decades. Thus, a natural question arises: whether the deeper-lying molecular orbitals play an important role in the generation of below- and near-threshold harmonics.

In this paper, we report unexplored evidence of multi-orbital contribution in the below- and near-threshold harmonic generation by performing a typical pump–probe experiment. From the abnormal behavior of the harmonic yield as a function of the time delay and crossing angle between the polarization directions of the pump and probe pulses, the contributing orbitals can be clearly identified. The results show that, compared with the above-threshold harmonic generation, the contribution of deeper-lying molecular orbitals could be much more prominent in the below- and near-threshold region, especially for harmonics closer to the ionization threshold. Further analysis indicates that the particular importance of the deeper-lying orbitals in this regime is closely related to the unique generation process initialized by the multi-photon excitation pathways instead of tunnel ionization. Our work can enrich people's understanding of the underlying mechanism of below- and near-threshold harmonic generation.

## 2. Experimental method

A typical pump–probe configuration is used in our experiments. The schematic layout of the experimental setup is shown in figure 1. We perform the experiment using a commercial Ti: sapphire laser system. It delivers a 35 fs, 800 nm pulse at a repetition rate of 1 kHz. The energy of our input pulse is 1 mJ, which has been split by a beam splitter into a pump arm to align molecules and a probe arm to generate harmonics. The pump and probe pulses are both linearly polarized. A wire

grid polarizer and two half-wave plates are used in both arms to continuously adjust the intensity and the polarization direction of the pulses. By stepping the pump arm with a motorized stage, the time delay between the pump and probe pulses is precisely controlled. In the end, both pulses are collinearly focused onto a supersonic gas jet by a silver-coated spherical mirror ($f = 100$ mm) to generate harmonics. Irises (not shown in figure 1 for conciseness) are used both in the alignment and driving arms to make sure the focal spot size of the alignment pulse is larger than that of the driving pulse. We optimized the phase-matching condition in our experiment to select the short trajectory by adjusting the position of the gas jet with respect to the focus. We confirm that the detected signals are dominated by the short-trajectory contribution according to their small divergent angle.

The generated harmonics are dispersed by a slit (0.1 mm wide and 15 mm high) and a flat-field grating (300 grooves mm$^{-1}$). Then the frequency-resolved harmonics are imaged onto a microchannel plate that is fitted with a phosphor screen of 90 mm diameter. Finally, the image of the generated harmonics is read out by a charge-coupled device. The yield of each harmonic is the spectral and spatial integral of the recorded image. In the below- and near-threshold regions, there exist some high-order diffractions from the higher-order harmonics. The ratio of high-order diffraction to its first-order diffraction can be estimated from the harmonic spectrum. Then, one can correctly obtain the harmonic yield of the ninth and the 11th harmonics by eliminating the contributions of the high-order diffractions. For the fifth harmonic, because of its weak harmonic signal, a better way to eliminate the contribution of high-order diffraction is to directly filter out the higher-order harmonic radiation. We installed a borosilicate film before the diffraction grating to filter out the radiation above the fifth order and get the fifth harmonic yield. The density and thickness of the film are 2.6989 g cm$^{-3}$ and 1.5 mm, respectively.

## 3. Experimental results and discussions

### 3.1. Delay dependence

Figure 2 shows the measured harmonic yield of nitrogen as a function of the time delay between the pump and probe pulses. The employed probe intensities from the top to the bottom are estimated to be $1.2 \times 10^{14}$ W cm$^{-2}$, $1.6 \times 10^{14}$ W cm$^{-2}$, $1.7 \times 10^{14}$ W cm$^{-2}$ and $1.8 \times 10^{14}$ W cm$^{-2}$, respectively. The employed pump intensity is fixed at $3.5 \times 10^{13}$ W cm$^{-2}$. The polarization axis of the probe pulse is parallel to that of the pump pulse. All the harmonic yields are normalized to that of unaligned nitrogen molecules under the same conditions. The ionization potential of HOMO in nitrogen is 15.5 eV, corresponding to 10 $\omega_0$, with $\omega_0$ being the probe laser frequency. Here, we present the results of the ninth and the 11th harmonics in the first two columns to show the characteristics of the below- and near-threshold harmonics. In addition, the results of plateau harmonic H17 and cutoff harmonics H31, H33, H35 and H37 for the respective employed laser intensity are presented for comparison.
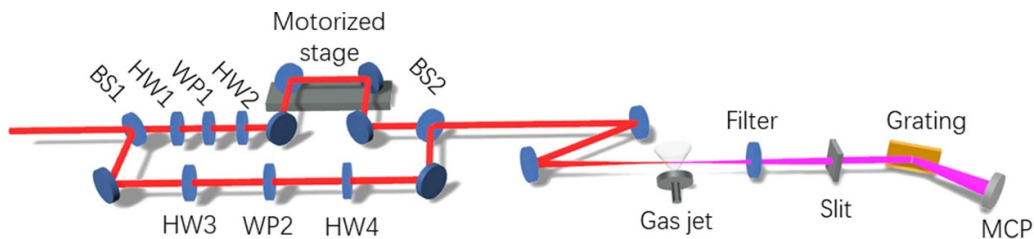
**Figure 1.** Schematic of the experimental setup. The typical pump–probe configuration is used in our experiments. The output pulses are split by a beam splitter (BS1) into a pump arm and a probe arm, and are finally collinear again at BS2. HW1 to HW4 are half-wave plates ($\lambda/2$ at 800 nm). WP1 and WP2 are wire grid polarizers. HW1(3) and WP1(2) are used to adjust the pump (probe) intensity. HW2(4) are used to adjust the polarization direction of the pump (probe) pulse. High-order harmonics are generated by focusing the pump and probe pulses with a spherical mirror ($f = 100$ mm) onto a gas jet. The time delay between the pump and probe pulses is precisely controlled by the motorized stage. The filter is used to get the fifth harmonic yield. Harmonics above the fifth order will be filtered out when it is installed before the diffraction grating.
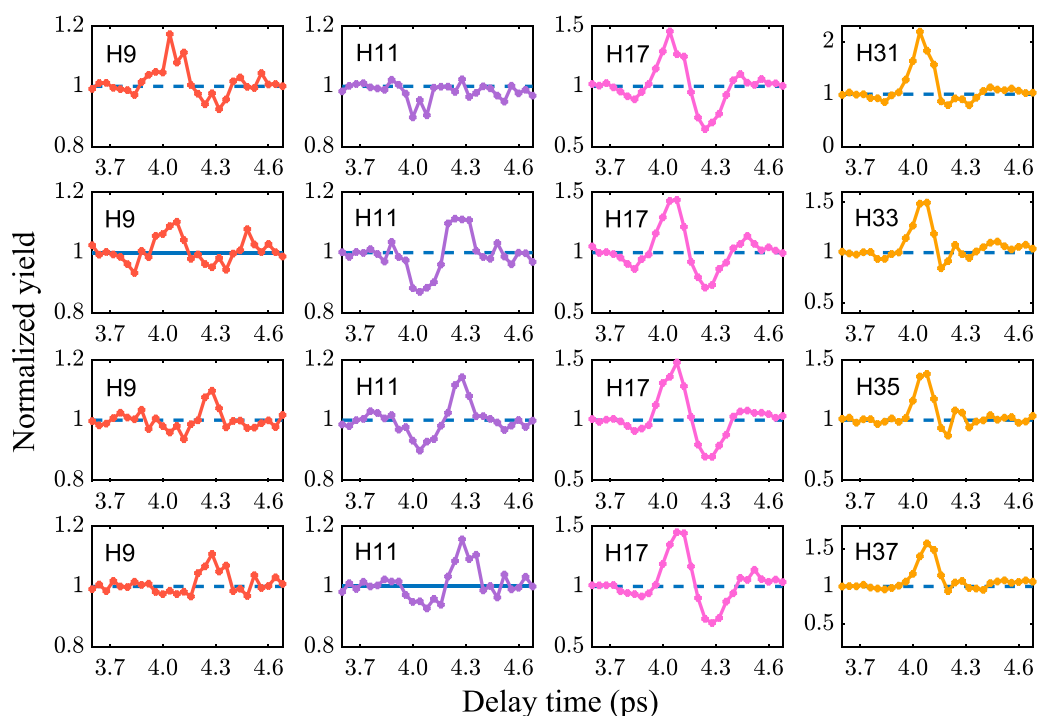


**Figure 2.** The harmonic yield as a function of the time delay between the pump and probe pulses. The pump intensity is fixed at $3.5 \times 10^{13}$ W cm$^{-2}$. The probe intensities from the top to the bottom are $1.2 \times 10^{14}$ W cm$^{-2}$, $1.6 \times 10^{14}$ W cm$^{-2}$, $1.7 \times 10^{14}$ W cm$^{-2}$ and $1.8 \times 10^{14}$ W cm$^{-2}$, respectively. The polarization axis of the pump pulse is parallel to that of the pump pulse. All harmonic yields are normalized to that of unaligned nitrogen molecules under the same condition.

As shown in figure 2, there exist distinctive differences among the characteristics of revival structure for harmonics in different regions. For the 17th harmonic, the revival structure shows the expected maximum at around 4.1 ps, where the molecules are aligned (the internuclear axis of nitrogen is parallel to the polarization direction of the pump pulse), and the expected minimum at around 4.3 ps, where the molecules are anti-aligned (the internuclear axis of nitrogen is perpendicular to the polarization direction of the pump pulse). However, for the cutoff harmonics, in addition to the maximum at around 4.1 ps, an additional small maximum arises at around 4.3 ps. Given the fact that nitrogen HOMO and HOMO-1 exhibit $\sigma_g$ and $\pi_\mu$ symmetries, respectively, the harmonic yield contributed by HOMO will monotonically decrease as the crossing

angle between the internuclear axis and the polarization axis of the probe pulse increases from 0° to 90°. On the contrary, the harmonic yield contributed by HOMO-1 will increase with the crossing angle. As a result, the pump–probe scan of the harmonic yield contributed by HOMO has a maximum at around 4.1 ps and a minimum at around 4.3 ps, while the harmonic yield contributed by HOMO-1 has a minimum at around 4.1 ps and a maximum at around 4.3 ps. Therefore, one can identify the contribution of different orbitals in the harmonic generation from the revival structure. The experimental observation shows that, as is well accepted, the plateau harmonic generation is dominated by HOMO, and HOMO-1 is responsible for the additional small maximum at around 4.3 ps for the cutoff harmonics [27, 29].
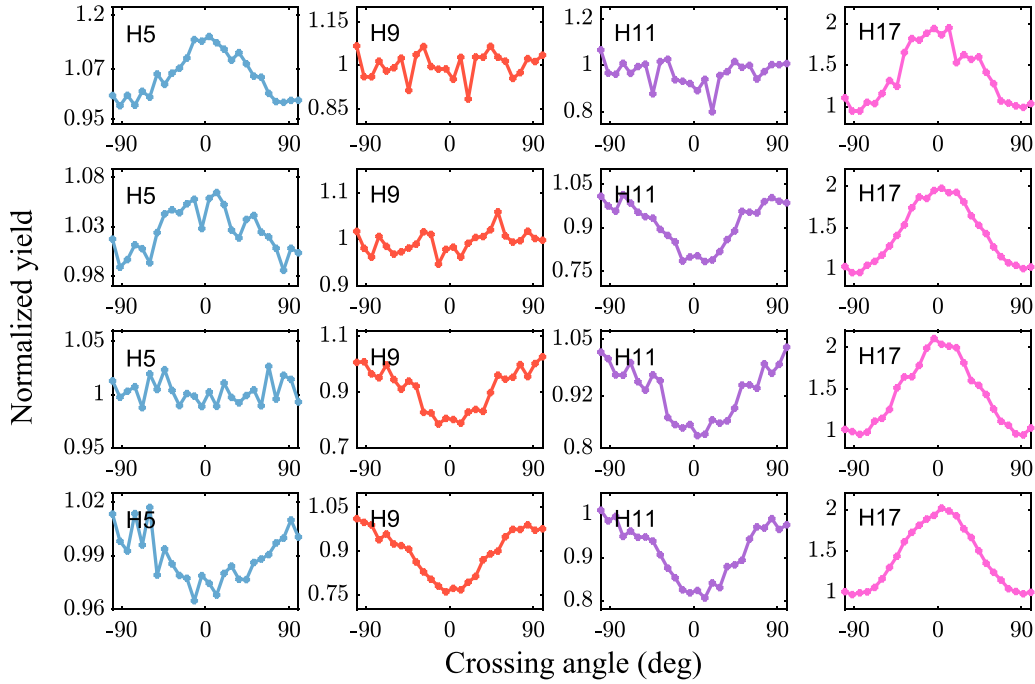
J. Phys. B: At. Mol. Opt. Phys. **56** (2023) 055601

J Long *et al*

**Figure 3.** The harmonic yield as a function of crossing angle $\theta$ between the polarization directions of the pump and probe pulses. The intensity of the pump pulse is fixed at $3.5 \times 10^{13}\,\mathrm{W\,cm^{-2}}$. The probe intensities from the top to the bottom are estimated to be $1.2 \times 10^{14}\,\mathrm{W\,cm^{-2}}$, $1.6 \times 10^{14}\,\mathrm{W\,cm^{-2}}$, $1.7 \times 10^{14}\,\mathrm{W\,cm^{-2}}$ and $1.8 \times 10^{14}\,\mathrm{W\,cm^{-2}}$, respectively. The time delay is fixed at 4.1 ps. All harmonic yields are normalized with respect to that of unaligned nitrogen molecules under the same condition.

Most interesting, however, is the abnormal revival structure of below- and near-threshold harmonics, which shows intensity-dependent modulation patterns. For the ninth harmonic, at the intensity of $1.2 \times 10^{14}\,\mathrm{W\,cm^{-2}}$, the revival structure exhibits the same characteristics as the plateau harmonics. That is, a maximum at around 4.1 ps is followed by a minimum at around 4.3 ps. However, as the intensity increases to $1.7 \times 10^{14}\,\mathrm{W\,cm^{-2}}$, the revival structure is inversed with a minimum at around 4.1 ps and a maximum at around 4.3 ps. For the 11th harmonic, the abnormal revival behavior becomes obvious even for weak intensity: the harmonic yield is almost consistent at the intensity of $1.2 \times 10^{14}\,\mathrm{W\,cm^{-2}}$, and the revival structure is inversed as the probe intensity increases to $1.6 \times 10^{14}\,\mathrm{W\,cm^{-2}}$.

As discussed above, one can identify the contributing orbitals in the harmonic generation from the revival structure. For the ninth harmonic, the same revival structure as plateau harmonics at $1.2 \times 10^{14}\,\mathrm{W\,cm^{-2}}$ suggests that the ninth harmonic generation is dominated by HOMO at weak intensity. However, as the probe intensity increases HOMO-1 begins to make an appreciable contribution and eventually dominates at strong intensity. HOMO-1 plays a more important role in the generation of the 11th harmonic, and shows the reversed revival structure at a lower probe intensity. It is worth mentioning that the absolute contribution of HOMO in the below- and near-threshold region increases with the probe intensity too, but the contribution of HOMO-1 increases more rapidly (as in detail discussed in section 4.2). As a result, HOMO-1 eventually

dominates the harmonic generation and leads to a reversed revival structure at higher probe intensity. These experimental results strongly suggest that HOMO-1 is critical for the generation of below- and near-threshold harmonics in nitrogen molecules. The contribution of HOMO-1 at anti-alignment can be much stronger than that of HOMO at alignment, resulting in an unexplored reversed revival structure.

### 3.2. Angle dependence

To further explore the harmonic generation in the below- and near-threshold regions, we present the harmonic yield as a function of the crossing angle $\theta$ between the polarization directions of the pump and probe pulses in figure 3. The experiment is performed under the same macroscopic conditions for figure 2. The results for H5, H9, H11 and H17 are presented. The polarization direction of the pump pulse is continuously rotated by a half-wave plate to adjust the crossing angle, and the time delay is fixed at 4.1 ps. All harmonic yields are normalized with respect to that of unaligned nitrogen molecules under the same conditions.

By comparing the first three columns with the last column, one can see that the yield of below- and near-threshold harmonics as a function of the crossing angle $\theta$ shows an intensity-dependent behavior, which is quite different from that of plateau harmonics. For the fifth harmonic, the modulation curve at the intensity of $1.2 \times 10^{14}\,\mathrm{W\,cm^{-2}}$ shows the expected shape as plateau harmonics, which monotonically decreases

as $|\theta|$ increases from $0°$ to $90°$, suggesting that the harmonic generation is dominated by HOMO. However, as the probe intensity increases, HOMO-1 begins to make an appreciable contribution to the harmonic generation at around $90°$, resulting in a flatter modulation curve of the total harmonic yield. When the intensity increases to $1.7 \times 10^{14}\,\mathrm{W\,cm^{-2}}$, the contribution of HOMO-1 at around $90°$ is comparable to that of HOMO at around $0°$, leading to an approximately isotropic total harmonic yield. Finally, when the probe intensity increases to $1.8 \times 10^{14}\,\mathrm{W\,cm^{-2}}$, the harmonic yield shows a reversed modulation curve, which increases with the crossing angle $|\theta|$ from $0°$ to $90°$, suggesting that the harmonic generation is dominated by HOMO-1. The same behavior of the modulation curve has been observed in the seventh (not shown), ninth and 11th harmonics, but the harmonic yield becomes approximately isotropic at lower intensities, which are $1.6 \times 10^{14}\,\mathrm{W\,cm^{-2}}$ and $1.2 \times 10^{14}\,\mathrm{W\,cm^{-2}}$ for the ninth and the 11th harmonics, respectively. This suggests that, in the below- and near-threshold region, HOMO-1 makes a greater relative contribution to harmonics closer to the ionization threshold at the same probe intensity.

Our experimental results strongly suggest that, compared with the above-threshold harmonic generation, HOMO-1 is more critical in the below- and near-threshold harmonic generation, resulting in the inversion of the harmonic yield as a function pump–probe delay and crossing angle $\theta$. Previous studies have demonstrated that the below- and near-threshold harmonic generation can be contributed by electrons initially excited through multi-photon excitation pathways and evolving closely around the core [35, 39]. Based on this unique generation mechanism, we propose that all the experimental observations can be well interpreted by the following physical picture. Specifically, the above-threshold harmonic generation is predominantly initialized by tunneling ionization, which exponentially depends on the ionization potential of the molecular orbital. In contrast, the exponential dependence turns into a power law in the multi-photon excitation situation [45, 46], which could be much less sensitive to the ionization potential. Thus, the contribution of deeper-lying orbitals could be more crucial in the below- and near-threshold harmonic generation than in the above-threshold region. Considering the angle dependence of the multi-photon processes, the contribution of deeper-lying orbitals to HHG can even surpass that of HOMO, leading to the observed inversion of the harmonic yield as a function pump–probe delay and crossing angle $\theta$ observed. On the other hand, HOMO generally dominates the plateau harmonic generation. Although the symmetry of molecular orbitals can increase the relative contribution of HOMO-1 for $|\theta| \approx 90°$, the yield of the 17th harmonic (as shown in figure 3) decreases as $|\theta|$ increases from $0°$ to $90°$, indicating that the plateau harmonic generation is dominated by the HOMO contribution. Even in the cutoff region, where the relative contribution of HOMO-1 can be further increased because of the wider harmonic spectrum of HOMO-1, the HOMO contribution for $|\theta| \approx 0°$ is still comparable to or stronger than that of HOMO-1 for $|\theta| \approx 90°$ [27].

## 4. Numerical calculation and analysis

### 4.1. Role of multi-orbital contribution

To validate the physical picture interpreting the experimental observations, we perform numerical simulations based on the two-dimensional time-dependent Schrödinger equation (TDSE), in which the potential of the target molecule is modeled by the soft-core potential

$$V(r) = -\sum_{\alpha=1,2} \frac{(Z_{\alpha i} - Z_{\alpha o})e^{-[(\mathbf{r}-\mathbf{R}_\alpha)^2/\rho]} + Z_{\alpha o}}{\sqrt{\xi + (\mathbf{r}-\mathbf{R}_\alpha)^2}} \quad (1)$$

where $\alpha = 1, 2$ labels the nuclei at fixed positions $\mathbf{R}_\alpha$. $Z_{\alpha i}$ and $Z_{\alpha o}$ denote the bare charge and the effective nuclear charge as seen by an electron at an infinite distance to the nuclei center. $\rho$ is the screening parameter, which characterizes the decrease in the effective charge of the nucleus with the distance. $\xi$ is the softening parameter to avoid infinity of $V(\mathbf{r})$ at the position of $\mathbf{r} = \mathbf{R}_\alpha$. In the case of nitrogen molecules, we take $Z_{1i} = 7$, $Z_{1o} = 0.5$, $\rho = 1.2$, and the internuclear distance $|\mathbf{R}_1 - \mathbf{R}_2| = 2.14$ a.u. We set the value of $\xi$ to be 1.204 and 1.122 for HOMO and HOMO-1, respectively. The orbitals are obtained by the imaginary time propagation. The corresponding calculated ionization potentials match the experimental values.

We use the split-operator method to solve the TDSE. At each time step, the time-dependent wave function $\psi(t)$ is multiplied by a mask function:

$$G(x,y) = g(x)g(y) \quad (2)$$

with

$$g(x) = \begin{cases} 1 & |x| < R-L \\ \sin^{1/8}\left(\frac{\pi(R-|x|)}{2L}\right) & |x| \geqslant R-L \end{cases} \quad (3)$$

and

$$g(y) = \begin{cases} 1 & |y| < R-L \\ \sin^{1/8}\left(\frac{\pi(R-|y|)}{2L}\right) & |y| \geqslant R-L \end{cases} \quad (4)$$

where $R$ and $L$ are the half-width of the simulation box and the width of the absorbing area (the area with $|x| \geqslant R-L$ and $|y| \geqslant R-L$), respectively. This is a computational trick widely used in solving the TDSE. Since the wave function in the absorbing area is absorbed, it can be used to avoid artificial reflections from the spatial boundaries of the simulation box due to its limited size. In this case, $R-L$ is generally much larger than the maximal displacement of the electron in the driving field. Moreover, in our study, such a computational trick can also be used to help explore the mechanism of below- and near-threshold harmonic generation, as one can separate the contributions of trajectories evolving closely around the core from others by setting the absorbing area at proper spatial positions [47, 48], as discussed in detail in section 4.2. Finally, the harmonic spectrum is obtained by the Fourier transform of the time-dependent dipole acceleration
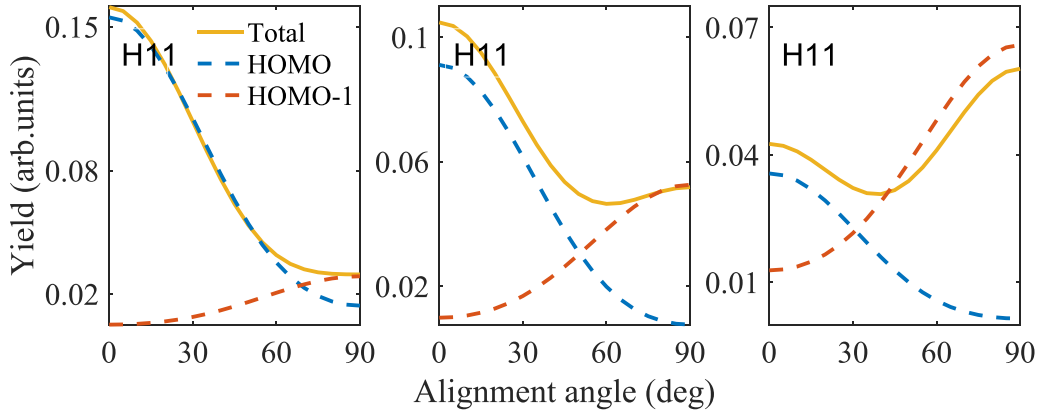
**Figure 4.** The simulated 11th harmonic yield of nitrogen in a linearly polarized laser field based on the TDSE method as a function of the alignment angle. The field intensities from the left panel to the right panel are $1.8 \times 10^{14} \, \text{W cm}^{-2}$, $2 \times 10^{14} \, \text{W cm}^{-2}$ and $2.2 \times 10^{14} \, \text{W cm}^{-2}$, respectively.
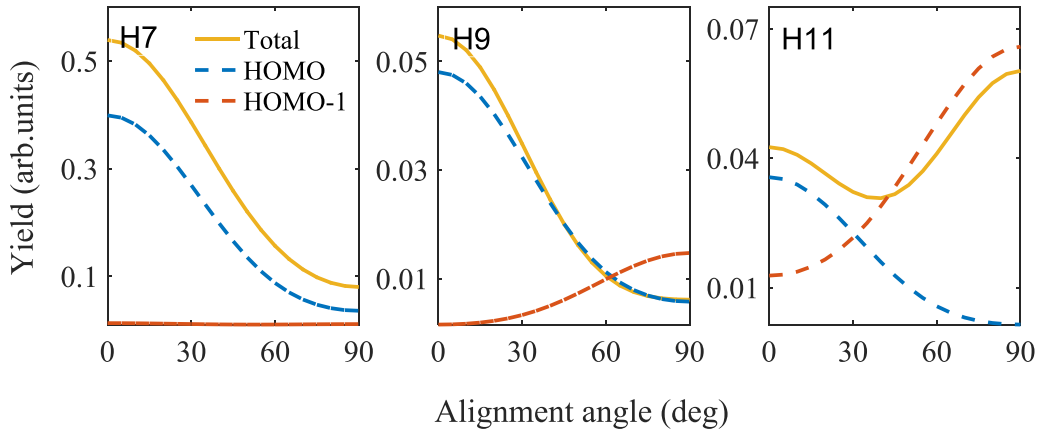


**Figure 5.** The simulated harmonic yield of nitrogen in a linearly polarized laser field based on the TDSE method for the seventh, ninth and 11th harmonics as a function of the alignment angle. The field intensity is $2.2 \times 10^{14} \, \text{W cm}^{-2}$.

$\langle \psi(t) || H(t), [H(t), q] || \psi(t) \rangle$ with $q = x, y$, respectively. More detailed information about the numerical calculation can be found in [49].

The yields of below- and near-threshold harmonics as a function of the alignment angle are simulated, where the alignment angle is the angle between the internuclear axis and the polarization direction of the applied laser field. Here, we present the result of the 11th harmonic in figure 4. The laser intensities from the left panel to the right panel are $1.8 \times 10^{14} \, \text{W cm}^{-2}$, $2.0 \times 10^{14} \, \text{W cm}^{-2}$ and $2.2 \times 10^{14} \, \text{W cm}^{-2}$, respectively. In addition, to take into account the effect of non-perfect alignment in experiments, an alignment distribution $\cos^2 \beta$ is considered in our simulation, where $\beta$ is the angle between the internuclear axis and the polarization direction of the alignment pulse. The total harmonic yield is the coherent superposition of the harmonic radiation contributed by HOMO and HOMO-1 at different $\beta$. At the intensity of $1.8 \times 10^{14} \, \text{W cm}^{-2}$, the contribution of HOMO-1 at around 90° is relatively much smaller than that of HOMO at around 0°. As a result, the total harmonic yield decreases as the alignment angle increases from 0° to 90°. When the probe intensity increases to $2 \times 10^{14} \, \text{W cm}^{-2}$, the contribution

of HOMO-1 becomes significant at around 90°, resulting in a flatter modulation curve of the total harmonic yield. As the probe intensity increases to $2.2 \times 10^{14} \, \text{W cm}^{-2}$, HOMO-1 gradually dominates the harmonic generation, leading to a reversed modulation curve. That is, the total harmonic yield increases with the alignment angle. The calculated results are in agreement with the experimental observation that the relative contribution of HOMO-1 is larger at a higher probe intensity.

Figure 5 shows the calculated harmonic yield as a function of the alignment angle at the intensity of $2.2 \times 10^{14} \, \text{W cm}^{-2}$. The results for the seventh, ninth and 11th harmonics are obtained. For the 11th harmonic, HOMO-1 gradually dominates the harmonic generation and the total yield shows a reversed modulation curve. However, for the seventh harmonic, the harmonic generation is dominated by HOMO, leading to the expected modulation curve of the total harmonic yield, which decreases with the alignment angle from 0° to 90°. Meanwhile, the total yield of the ninth harmonic begins to show the additional maximum contributed by HOMO-1 at around 90°. These calculated results are in agreement with the experimental observation that, in the
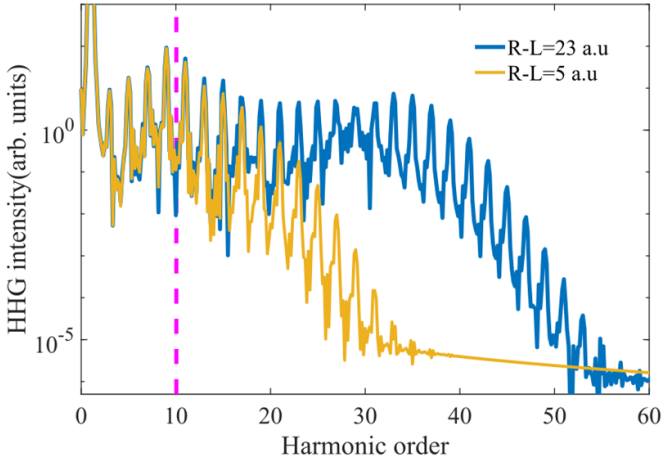
**Figure 6.** High-order harmonic spectra for HOMO of nitrogen aligned along the polarization of the driving laser field corresponding to $R - L = 5$ a.u (yellow solid line) and 23 a.u (blue solid line), respectively. The vertical dashed line marks the position of the ionization potential of HOMO. The field intensity is $2.0 \times 10^{14}\,\mathrm{W\,cm^{-2}}$.
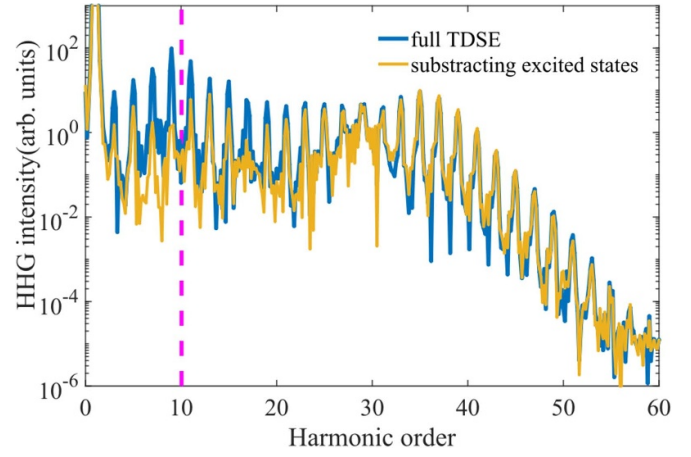


**Figure 7.** High-order harmonic spectra for HOMO of nitrogen obtained by full TDSE calculation (blue solid line) and by subtracting the projection on excited states (yellow solid line). The nitrogen is aligned along the direction of the driving laser field. The vertical dashed line marks the position of the ionization potential of HOMO. The field intensity is $2.0 \times 10^{14}\,\mathrm{W\,cm^{-2}}$.

below- and near-threshold region, the contribution of HOMO-1 is more significant for harmonics closer to the ionization threshold.

### 4.2. Role of multi-photon excitation pathways

To further examine the generation mechanism of the below- and near-threshold harmonics and verify why the deeper-lying harmonics are particularly important, we first perform the HHG calculation by shrinking the simulation box while keeping the width of the absorbing area constant. As $R$ decreases, the contribution of continuum electrons is suppressed, and meanwhile one can see that harmonics with higher orders decrease dramatically. On the other hand, the below- and near-threshold harmonics are unchanged even at very small $R - L$. Two typical results with $R - L = 5$ a.u. and 23 a.u. for the HOMO of nitrogen aligned along the direction of the laser field are shown in figure 6, where we set the width of the absorbing area $L = 28.2$ a.u. As demonstrated in previous works, while the long trajectory for below- and near-threshold harmonic generation can be understood similarly to the standard three-step picture of HHG, the short trajectory is dominated by electrons initially excited through multi-photon excitation pathways and evolves closely around the core, generating harmonics even without requiring ionization [39]. Our results with different $R - L$ are well consistent with the latter mechanism and confirm that the obtained harmonics below and near the ionization threshold are predominantly generated via the short trajectory, involving multi-photon excitation. From an alternative perspective, one may also understand that the harmonics can be generated, while bound electrons are polarized under an oscillating external laser field. The result that the short trajectory dominates the low-order harmonics over the long trajectory is consistent with that in [35] and with our experimental observation.

We also cross-validate the generation mechanism by performing the calculation in a different way. We subtract the projection on excited states $\phi_i$ from the time-dependent wave function $\psi(t) \rightarrow \psi(t) - \sum_i \langle \phi_i | \psi(t) \rangle | \phi_i \rangle$ at each time step in the TDSE calculation, so that the contribution of multi-photon excitation pathways is suppressed. The result for the HOMO of nitrogen aligned along the direction of the laser field is shown in figure 7, where three of the most populated excited states (accounting for more than 94% of the whole excitation) are subtracted. One can see that the below- and near-threshold harmonic generation is significantly suppressed when we remove these intermediate states, while harmonics with higher energies are almost unaffected. These results, from another side, indicate that the excited states play a significant role in the generation of below- and near-threshold harmonics via the multi-photon excitation pathways [39, 50]. The above conclusions hold true for HOMO-1 too.

The difference in the generation mechanisms will be reflected in the relative contribution of deeper-lying orbitals. One significant difference is the dependence of the ionization or excitation rate on the ionization potential $I_p$. The tunneling rate depends on $I_p$ sensitively in an exponential manner as $\sim \exp\left(-\frac{2}{3}\frac{(2I_p)^{3/2}}{F}\right)$ ($F$ is the laser field), while in the multi-photon regime the dependence turns to a power law involving the number of absorbed photons [45, 46]. The latter dependence can be much flatter than the former. As a result, compared with the above-threshold harmonic generation, the contribution of deeper-lying orbitals could be comparable to that of HOMO and be of particular importance in the below- and near-threshold region. Considering the angle dependence of multi-photon processes, the contribution of deeper-lying orbitals can even surpass that of HOMO and lead to the inversion of the harmonic yield as a function of pump–probe delay and crossing angle $\theta$ as shown in figures 2 and 3.

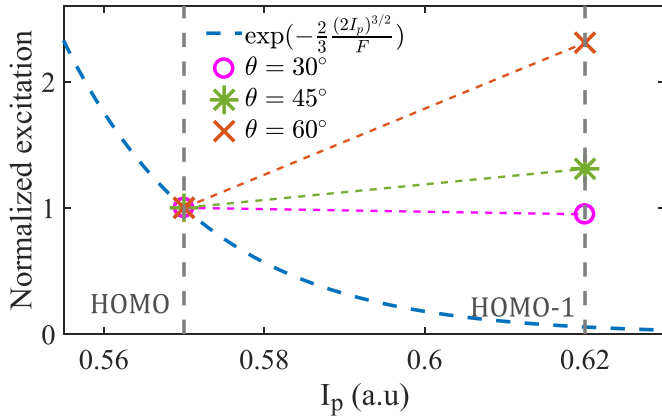**Figure 8.** The normalized time-averaged population of excited states for HOMO and HOMO-1 of nitrogen aligned at $\theta = 30°$ (circle), $45°$ (star), $60°$ (cross), respectively. The field intensity is $2.0 \times 10^{14} \, \text{W cm}^{-2}$.



**Figure 9.** The ratio of time-averaged population of excited states for HOMO-1 aligned at $\theta = 90°$ to that for HOMO aligned at $\theta = 0°$.

To examine this picture, we calculate the time-average of the population of excited states $\sum_i |\langle \phi_i | \psi(t) \rangle|^2$ for initial states HOMO and HOMO-1 at different alignment angles $\theta = 30°$, $45°$, $60°$, respectively. The results are shown in figure 8. For comparison, we also mimic the exponentially dependent tunnel ionization with $\exp(-\frac{2}{3} \frac{(2I_\text{p})^{3/2}}{F})$. All the results are normalized so that the excitation or ionization of HOMO is 1. As shown in figure 8, the population of excited states for HOMO-1 is comparable to that for HOMO at $\theta = 30°$, while the tunnel ionization dramatically decreases for the deeper HOMO-1. Moreover, one can see that the population of excited states for HOMO-1 is even relatively higher than that for HOMO at $45°$ and $60°$, respectively, consistent with the expected angle dependence of the multi-photon excitation paths for HOMO and HOMO-1. All the results in figure 8 show that the contribution of HOMO-1 can be of particular importance via the unique multi-photon excitation paths for below- and near-threshold harmonic generation. Note that, except for the symmetry of the initial state, the excitation also depends on the symmetry of the excited states. The symmetry selection rule determines the angle dependence of both the excitation process and the harmonic generation by the excited states. Taking HOMO driven by linearly polarized laser fields, for example, the excitation is maximum at $\theta = 0°$ and minimum at $\theta = 90°$. At the same time, the harmonic generation contributed by the excited intermediate states would also be preferred at $\theta = 0°$ and be suppressed for $\theta = 90°$ too.

Another interesting phenomenon, found both in the experiments and numerical calculation, is that the contribution of HOMO-1 at $90°$ increases with the laser intensity faster than that of HOMO at $0°$. This is because the difference between the excitation probabilities to intermediate states from HOMO and HOMO-1 becomes smaller for stronger driving lasers. As a result, the HOMO-1 contribution relative to that of HOMO becomes more important at higher intensity. To confirm this, we calculate the time-averaged population of intermediate excited states corresponding to HOMO-1 at $90°$ and HOMO at $0°$ at various intensities. As shown in figure 9, the ratio of the population of the excited states
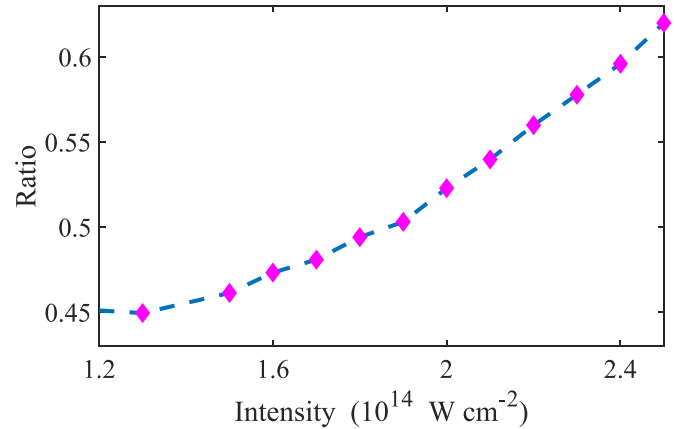
for HOMO-1 to that for HOMO increases with the laser intensity.

## 5. Conclusion

In conclusion, we have experimentally demonstrated that the deeper-lying orbitals are crucial for the generation of below- and near-threshold harmonics. Specifically, by scanning the time delay and the crossing angle of polarization directions between the pump pulse and the probe pulse, we find that the harmonic yield in the below- and near-threshold region shows flattened or even reversed modulation patterns with respect to that of plateau harmonics. Further comparison and analysis indicate that, for below- and near-threshold harmonic generation in a strong field, the HOMO-1 contribution can overall surpass the HOMO contribution, especially for harmonics closer to the ionization threshold. The particular importance of the deeper-lying orbitals in this regime is more closely related to the flatter ionization potential dependence of the multi-photon excitation pathways involved in the generation process, rather than tunnel ionization. Our study may be beneficial for further investigations to reveal the mechanism of harmonic generation of the below- and near-threshold harmonics.

J. Phys. B: At. Mol. Opt. Phys. 56 (2023) 055601

J Long *et al*

## ORCID iDs

Jie Long  🔵 https://orcid.org/0000-0002-0790-8199
Xiaosong Zhu  🔵 https://orcid.org/0000-0003-4289-9993

## References

[1] Li J *et al* 2017 53-attosecond x-ray pulses reach the carbon K-edge *Nat. Commun.* **8** 186
[2] Medišauskas L, Wragg J, van der Hart H and Ivanov M Y 2015 Generating isolated elliptically polarized attosecond pulses using bichromatic counterrotating circularly polarized laser fields *Phys. Rev. Lett.* **115** 153001
[3] Kfir O *et al* 2015 Generation of bright phase-matched circularly-polarized extreme ultraviolet high harmonics *Nat. Photon.* **9** 99
[4] Fan T *et al* 2015 Bright circularly polarized soft x-ray high harmonics for x-ray magnetic circular dichroism *Proc. Natl, Acad. Sci. USA* **112** 14206
[5] Willems S, Smeenk C T L, Zhavoronkov N, Kornilov O, Radu I, Schmidbauer M, Hanke M, von Korff Schmising C, Vrakking M J J and Eisebitt S 2015 Probing ultrafast spin dynamics with high-harmonic magnetic circular dichroism spectroscopy *Phys. Rev.* B **92** 220405(R)
[6] Lan P *et al* 2017 Attosecond probing of nuclear dynamics with trajectory-resolved high-harmonic spectroscopy *Phys. Rev. Lett.* **119** 033201
[7] Corkum P B 1993 Plasma perspective on strong field multiphoton ionization *Phys. Rev. Lett.* **71** 1994
[8] Schafer K J, Yang B, DiMauro L F and Kulander K C 1993 Above threshold ionization beyond the high harmonic cutoff *Phys. Rev. Lett.* **70** 1599
[9] Alnaser A S, Voss S, Tong X, Maharjan C M, Ranitovic P, Ulrich B, Osipov T, Shan B, Chang C and Cocke C L 2004 Effects of molecular structure on ion disintegration patterns in ionization of $O_2$ and $N_2$ by short laser pulses *Phys. Rev. Lett.* **93** 113003
[10] Pavičić D, Lee K F, Rayner D M, Corkum P B and Villeneuve D M 2007 Direct measurement of the angular dependence of ionization for $N_2$, $O_2$ and $CO_2$ in intense laser fields *Phys. Rev. Lett.* **98** 243001
[11] Levesque J, Mairesse Y, Dudovich N, Pépin H, Kieffer J C, Corkum P B and Villeneuve D M 2007 Polarization state of high-order harmonic emission from aligned molecules *Phys. Rev. Lett.* **99** 243001
[12] Lee G H, Kim I J, Park S B, Kim T K and Nam C H 2008 Measurement of the polarization of high-order harmonics from aligned $N_2$ molecules by spatial interferometry *Opt. Lett.* **33** 2083
[13] Itatani J, Levesque J, Zeidler D, Niikura H, Pépin H, Kieffer J C, Corkum P B and Villeneuve D M 2004 Tomographic imaging of molecular orbitals *Nature* **432** 867
[14] Haessler S, Caillat J and Salières P 2011 Self-probing of molecules with high harmonic generation *J. Phys. B: At. Mol. Opt. Phys.* **44** 203001
[15] Baker S, Robinson J S, Haworth C A, Teng H, Smith R A, Chirila C C, Lein M, Tisch J W G and Marangos J P 2006 Probing proton dynamics in molecules on an attosecond time scale *Science* **312** 424
[16] Baykusheva D, Ahsan M S, Lin N and Wörner H J 2016 Bicircular high-harmonic spectroscopy reveals dynamical symmetries of atoms and molecules *Phys. Rev. Lett.* **116** 123001
[17] He L, Lan P, Le A-T, Wang B, Wang B, Zhu X, Lu P and Lin C D 2018 Real-time observation of molecular spinning with angular high-harmonic spectroscopy *Phys. Rev. Lett.* **121** 163201
[18] He L *et al* 2018 Monitoring ultrafast vibrational dynamics of isotopic molecules with frequency modulation of high-order harmonics *Nat. Commun.* **9** 1108
[19] Shiner A D, Schmidt B E, Trallero-Herrero C, Wörner H J, Patchkovskii S, Corkum P B, Kieffer J-C, Légaré F and Villeneuve D M 2011 Probing collective multi-electron dynamics in xenon with high-harmonic spectroscopy *Nat. Phys.* **7** 464
[20] Huang Y *et al* 2021 Ultrafast hole deformation revealed by molecular attosecond interferometry *Ultrafast Sci.* **2021** 9837107
[21] Bertrand J B, Wörner H J, Salières P, Villeneuve D M and Corkum P B 2013 Linked attosecond phase interferometry for molecular frame measurements *Nat. Phys.* **9** 174
[22] Ferré A *et al* 2015 Multi-channel electronic and vibrational dynamics in polyatomic resonant high-order harmonic generation *Nat. Commun.* **6** 5952
[23] Santra R and Gordon A 2006 Three-step model for high-harmonic generation in many-electron systems *Phys. Rev. Lett.* **96** 073906
[24] Patchkovskii S, Zhao Z, Brabec T and Villeneuve D M 2006 High harmonic generation and molecular orbital tomography in multielectron systems: beyond the single active electron approximation *Phys. Rev. Lett.* **97** 123003
[25] Sukiasyan S, McDonald C, Destefani C, Ivanov M Y and Brabec T 2009 Multielectron correlation in high-harmonic generation: a 2D model analysis *Phys. Rev. Lett.* **102** 223002
[26] Xia Y and Jaroń-Becker A 2014 Multielectron contributions in elliptically polarized high-order harmonic emission from nitrogen molecules *Opt. Lett.* **39** 001461
[27] Troß J, Ren X, Makhija V, Mondal S, Kumarappan V and Trallero-Herrero C A 2017 $N_2$ HOMO-1 orbital cross section revealed through high-order-harmonic generation *Phys. Rev.* A **95** 033419
[28] Haessler S *et al* 2010 Attosecond imaging of molecular electronic wavepackets *Nat. Phys.* **6** 200
[29] Mcfarland B K, Farrell J P, Bucksbaum P H and Gühr M 2008 High harmonic generation from multiple orbitals in $N_2$ *Science* **322** 1232
[30] Smirnova O, Mairesse Y, Patchkovskii S, Dudovich N, Villeneuve D, Corkum P and Ivanov M Y 2009 High harmonic interferometry of multi-electron dynamics in molecules *Nature* **460** 972
[31] Shu Z, Liang H, Wang Y, Hu S, Chen S, Xu H, Ma R, Ding D and Chen J 2022 Channel coupling dynamics of deep-lying orbitals in molecular high-harmonic generation *Phys. Rev. Lett.* **128** 183202
[32] Li P-C, Sheu Y-L, Laughlin C and Chu S-I 2015 Dynamical origin of near- and below-threshold harmonic generation of Cs in an intense mid-infrared laser field *Nat. Commun.* **6** 7178
[33] Xiong W, Geng J, Tang J, Peng L and Gong Q 2014 Mechanisms of below-threshold harmonic generation in atoms *Phys. Rev. Lett.* **112** 233001
[34] Yost D C, Schibli T R, Ye J, Tate J L, Hostetter J, Gaarde M B and Schafer K J 2009 Vacuum-ultraviolet frequency combs from below-threshold harmonics *Nat. Phys.* **5** 815
[35] Hostetter J A, Tate J L, Schafer K J and Gaarde M B 2010 Semiclassical approaches to below-threshold harmonics *Phys. Rev.* A **82** 023401
[36] Li P-C, Sheu Y-L, Laughlin C and Chu S-I 2014 Role of laser-driven electron-multirescattering in resonance-enhanced below-threshold harmonic generation in He atoms *Phys. Rev.* A **90** 041401
[37] Chini M *et al* 2014 Coherent phase-matched VUV generation by field-controlled bound states *Nat. Photon.* **8** 437

J. Phys. B: At. Mol. Opt. Phys. **56** (2023) 055601

J Long *et al*

[38] Xiong W, Xiao X, Peng L and Gong Q 2016 Correspondence of below-threshold high-order-harmonic generation and frustrated tunneling ionization *Phys. Rev.* A **94** 013417

[39] Soifer H, Botheron P, Shafir D, Diner A, Raz O, Bruner B D, Mairesse Y, Pons B and Dudovich N 2010 Near-threshold high-order harmonic spectroscopy with aligned molecules *Phys. Rev. Lett.* **105** 143904

[40] Burnett N H, Kan C and Corkum P B 1995 Ellipticity and polarization effects in harmonic generation in ionizing neon *Phys. Rev.* A **51** R3418

[41] Kakehata M, Takada H, Yumoto H and Miyazaki K 1997 Anomalous ellipticity dependence of high-order harmonic generation *Phys. Rev.* A **55** R861

[42] Wang B, Zhang Y, Lan P, Zhai C, Li M, Zhu X, Chen J, Lu P and Lin C D 2021 Anomalous ellipticity dependence of the generation of near-threshold harmonics in noble gases *Phys. Rev.* A **103** 053119

[43] Ferré A *et al* 2014 A table-top ultrashort light source in the extreme ultraviolet for circular dichroism experiments *Nat. Photon.* **9** 93

[44] Power E P, March A M, Catoire F, Sistrunk E, Krushelnick K, Agostini P and DiMauro L F 2010 XFROG phase measurement of threshold harmonics in a Keldysh-scaled system *Nat. Photon.* **4** 352–6

[45] Ivanov M Y, Spanner M and Smirnova O 2005 Anatomy of strong field ionization *J. Mod. Opt.* **52** 165

[46] Keldysh L V 1965 Ionization in the field of a strong electromagnetic wave *J. Exp. Theor. Phys.* **20** 1307

[47] Yu S, Dong F, Xu R, Li W, Wang S and Chen Y 2019 Suppressed short-trajectory near-threshold harmonics as a sign of tunnel exit *J. Phys. B: At. Mol. Opt. Phys.* **52** 085001

[48] Xu R, Chen Y, Liu J and Fu L 2016 Tracking origins of below-threshold harmonics with a trajectory-resolved fully quantum approach *Phys. Rev.* A **94** 063417

[49] Sun N, Zhu X, Wang B, Wang D, Shao R, Lan P and Lu P 2020 Near-circularly-polarized attosecond pulse generation from carbon monoxide molecules with a combination of linearly and circularly polarized fields *Phys. Rev.* A **101** 053437

[50] Botheron P and Pons B 2010 Self-consistent Bohmian description of strong field-driven electron dynamics *Phys. Rev.* A **82** 021404(R)